


Hydrodynamics and contaminant transport on a degraded bed at a 90-degree channel confluence

Hongwu Tang¹ · Huiming Zhang²  · Saiyu Yuan¹

Received: 16 November 2016 / Accepted: 12 November 2017 / Published online: 18 November 2017
© Springer Science+Business Media B.V., part of Springer Nature 2017

Abstract Channel confluences at which two channels merge have an important effect on momentum exchange and contaminant diffusion in both natural rivers and artificial canals. In this study, a three-dimensional numerical model, which is based on the Reynolds Averaged Navier–Stokes equations and Reynolds Stress Turbulence model, is applied to simulate and compare flow patterns and contaminant transport processes for different bed morphologies. The results clearly show that the distribution of contaminant concentrations is mainly controlled by the shear layer and two counter-rotating helical cells, which in turn are affected by the discharge ratio and the bed morphology. As the discharge ratio increases, the shear flow moves to the outer bank and the counter-clockwise tributary helical cell caused by flow deflection is enlarged, leading the mixing happens near the outer bank and the mixing layer distorted. The bed morphology can induce shrinkage of the separation zone and increase of the clockwise main channel helical cell, which is initiated by the interaction between the tributary helical cell and the main channel flow and strengthened by the deep scour hole. The bed morphology can also affect the distortion direction of the mixing layer. Both a large discharge ratio and the bed morphology could lead to an increase in mixing intensity.

Keywords Hydrodynamics · Contaminant transport · Bed morphology · Channel confluence

✉ Hongwu Tang
hwtang@hhu.edu.cn

¹ State Key Laboratory of Hydrology-Water Resources and Hydraulic Engineering, Hohai University, Nanjing 210098, China

² State Key Laboratory of Hydrology-Water Resources and Hydraulic Engineering, College of Water Conservancy and Hydropower Engineering, Hohai University, Nanjing 210098, China

1 Introduction

Open channel confluences are a common component of both natural rivers and artificial canals. The flow patterns at confluences affect not only the temporal and spatial distribution of contaminants in the river networks, but also the bed morphology at confluences. The hydrodynamic characteristics at an open channel confluence are shown in Fig. 1. At the upstream junction corner, a stagnation zone develops due to the reduction of the velocity of the mainstream flow. The flow originating from the tributary channel deflects towards the downstream channel, and a shear layer is formed at the interface between mainstream and tributary flows. At the downstream junction corner, the tributary flow detaches from and reattaches to the bank at some distance downstream, causing the formation of a separation zone. Adjacent to the separation zone, the confluent flows pass through a narrowed area, thus, leading to an increase in velocity [1]. At the downstream of the separation zone is the flow recovery zone, where the velocities of tributary and mainstream flows are comparable, and thus the flow shear between them disappears. The discharge ratio, q , the junction angle between the tributary and the main channel, α , and the bed morphology are recognized to be the main factors affecting the flow characteristics and mixing process at channel confluences [2–5].

Previous studies on the hydrodynamics at river confluences have focused on the flow structure and possible factors affecting flow characteristics, such as discharge ratio, confluence angle and bed discordance. The first effort to develop a general model of the hydrodynamics at river confluences was made by Best. Six major zones were identified at channel confluences, and the dominant controls on these zones were the confluence angle and discharge ratio [2–4, 6]. Best and Reid [6] found that as the confluence angle or the discharge ratio increased, the width and length of the separation zone increased, but its shape index (the maximum width-to-length ratio) remained almost constant. Yang et al. [7] showed that the isoline method, in which the border of the separation zone was depicted using the zero-longitudinal velocity isoline, was more physically accurate than the commonly used streamline method, in which the border of the separation zone was depicted using a streamline starting from the downstream junction corner and ending at the intersection point. A significant feature at a confluence is the flow shear between the two convergent flows, which is characterized by vertical eddies in the mixing interface and streamwise-oriented vortical (SOV) cells adjacent to the mixing interface [8, 9]. These vortices are responsible for the increase in bed shear stress and velocity at confluences as flows merge together, resulting in considerable bed scour [3, 10]. However, the SOV cells may enhance the bed shear stress to a greater degree than the vertical eddies in the mixing

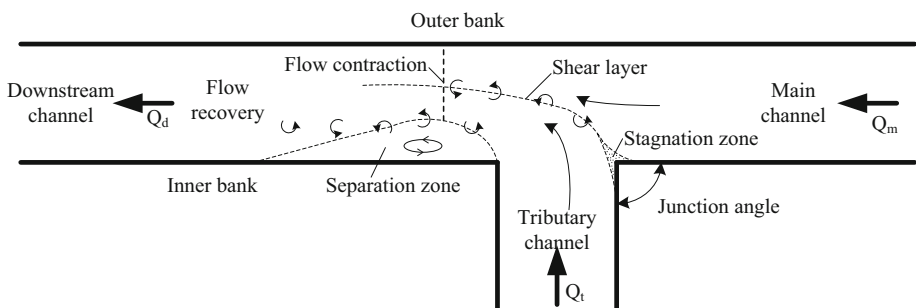


Fig. 1 A conceptual model of flow characteristics at an open channel confluence (after Best [2])

interface [8]. The field studies of Biron et al. [11] and Rhoads and Sukhodolov [12] investigated the shear layer at natural river confluences by using time series and spectral analyses of velocity data collected at a relatively high sampling frequency. Yuan et al. [13] investigated the flow structure in the distorted shear layer at a channel confluence with a small width-to-depth ratio, and found that the strong helical cells were helpful for the mixing of contaminants. Shakibainia et al. [14] observed three kinds of helical cells, including separation zone, tributary channel, and main channel helical cells. The separation zone helical cell owes its formation to the separation zone, but it may be absent in natural rivers due to sediment deposition in this region. The tributary helical cell originating from the deflection of the tributary flow is the strongest helical cell at confluences. The main channel helical cell is initiated by the interaction between the tributary helical cell and the main channel flow. These helical cells can become stronger and more distinguishable as the confluence angle and the discharge ratio increase [14]. The effect of bed discordance, a common feature of most river confluences, on the hydrodynamics at confluences was discussed by Biron et al. [5], De Serres et al. [15], Bradbrook et al. [16], Wang and Yan [17] and Boyer et al. [18]. The deflection of main channel flow may disappear because of bed discordance, and the shear layer between the two confluent flows is distorted towards the shallower tributary channel, resulting in fluid upwelling from the deeper main channel into the shallower tributary channel, and the flow separation zone is absent close to the bed but present near the water surface.

Bed morphology at channel confluences is characterized by bed discordance between the tributary and main channel, bed scour region at the middle of the confluence zone, and bar in the downstream channel originated from the formation of the separation zone at the downstream junction corner [4]. However, the influence of bed morphology on flow structure at channel confluences remains to be clarified. Furthermore, there have been few studies on the transport of suspended and dissolved contaminants at channel confluences. The mixing rate at the downstream of the junction has been used to explain the mixing processes at confluences. According to Jirka [19], regardless of potential amplifications and complexities, complete vertical mixing is a rapid process with maximal mixing distance of a few tens of the water depth, while complete lateral mixing requires large distances. For typical river morphology with a channel width-to-depth ratio ranging from 10 to 100, complete mixing requires a distance of 100–1000 river widths. However, Gaudet and Roy [20] observed much faster mixing (around 25 channel widths) at discordant bed confluences with widths ranging from 5 to 15 m, which could be attributed to the distortion of the mixing layer as the flow originating from the shallower tributary tended to flow over the flow originating from the deeper main channel [20, 21]. Mignot et al. [22] used a so-called Serret-Frenet frame-axis based on the local direction of the velocity to describe the shape of the mixing layer. They found that the centerline of the mixing layer fairly fitted the streamline separating at the upstream corner, and the shape of the mixing layer seemed to be strongly affected by streamwise acceleration.

Both field observations and laboratory experiments have contributed to our understanding of flow patterns and mixing at channel confluences. However, currently used flow measurement equipment does not enable the detection of sophisticated flow structures. Thus, many researchers use numerical models as a complementary technique to explore the exchange mechanism and the relative importance of different control factors at confluences. Mcguirk and Rodi [23] used a two-dimensional depth averaged model with a rigid lid and a basic two-equation turbulence model (k - ϵ model) to simulate the problem of a side discharge into open channel flow. Weerakoon and Tamai [24] also used the basic two-equation turbulence model with a rigid lid to simulate flow characteristics at channel

confluences. However, a parabolic treatment can severely limit the applicability of these models to confluences with no recirculation. Later, Weerakoon et al. [25] modified the model by adopting a fully elliptic treatment for a 60-degree confluence. They made a qualitative comparison of the flow patterns at the bed and surface, and concluded that the numerical predictions agreed reasonably well with the experimental results. Three-dimensional (3D) numerical modelling has been used successfully to investigate the mixing patterns by simulating a numerical tracer subject to advection by the mean flow and turbulent diffusion [16, 26, 27].

Thus, the purpose of this study is to investigate the effects of bed morphology on the hydrodynamics and the transport of contaminants on degraded beds at 90-degree channel confluences by using a 3D numerical model, which is based on Reynolds Averaged Navier–Stokes Equations solved using a Reynolds Stress Turbulence model, and the results are then validated by laboratory experimental data.

2 Numerical modeling and verification

2.1 Laboratory experiments for numerical model validation

Bed morphology and velocity data are collected from laboratory experiments performed in a 90-degree confluence flume, as shown in Fig. 2. All channels are horizontal with a rectangular cross section. The tributary and main channels are 30 cm wide and 3 m long, while the post-confluence channel is extended to 40 cm wide and 7 m long. It is common for the post-confluence channel to be slightly wider than the tributary or main channel at natural river confluences, which is referred to as “downstream hydraulic geometry” [28]. There are water tanks at the head of the two upstream channels and the end of the downstream channel. The two upstream water tanks are connected with the downstream tank using polyvinyl chloride pipes. The flow discharges of both upstream channels are precisely monitored by two ultrasonic flowmeters and valves. Honey combs are installed at the entrance of the flume to help the flow become fully developed as soon as possible, and the water level is adjusted using the tail gate downstream of the flume ($h = 22$ cm). In this study, for the purpose of getting a stable degraded bed morphology, the experiments were conducted under clear-water conditions (i.e., no suspended or bedload sediment was added), and the sediment should satisfy the following criteria: (1) there is hardly any incipient sediment motion in the two upstream channels, and only a small amount of moving sediment in the downstream channel; (2) a typical bed morphology involving scour holes and bars should develop in the confluent zone; and (3) a perfect armoring after the erosion of fine sediment should be formed. Thus, poorly sorted sediment is used as the bed material, where $d_{50} = 0.9$ mm, $d_{90} = 2.5$ mm, and its sorting coefficient is $\sigma = 0.5(d_{84}/d_{50} + d_{50}/d_{16}) = 2.41$, where d_x is the diameter with x percent of the sediment finer than this size.

Two discharge ratios are considered in this study. In Case 1, the discharge of the tributary channel, Q_t , is 6.0 L/s, and that of the main channel, Q_m , is 9.0 L/s, yielding a discharge ratio, $q = Q_t/Q_m$, of 2/3. In Case 2, Q_t is 9.0 L/s and Q_m is 6.0 L/s, yielding a discharge ratio of 3/2. The total downstream discharge Q_d is kept constant at 15.0 L/s in both experiments. In Cases 1 and 2, the bed was initially covered with a 6-cm-thick layer of poorly sorted sediments. As water flowed through the confluent zone, fine sands were more likely to be eroded, forming a coarser layer to protect finer sands beneath it from being

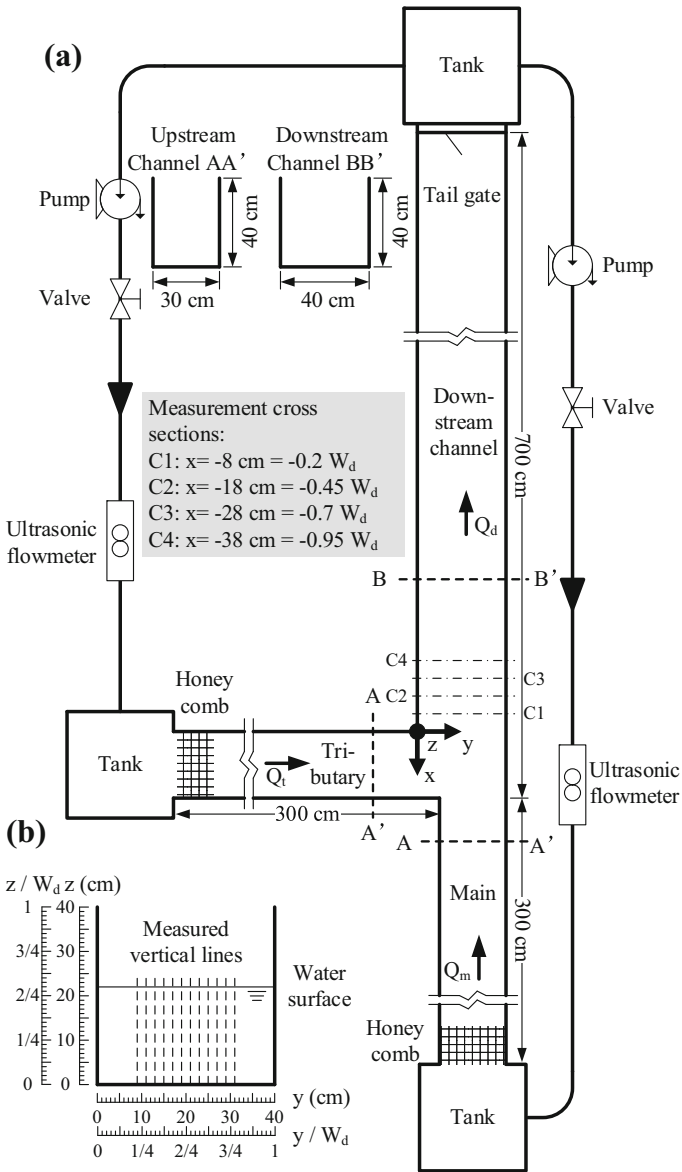


Fig. 2 A schematic of the confluence channel flume with a 90-degree junction angle (where x = stream-wise direction of the main channel measured upstream of the downstream confluence point, y = lateral distance across the channels, z = the elevation above the channel bed, W_d = width of the downstream channel)

eroded, which is referred to as ‘armoring’ process. Equilibrium was determined based on the change in bed morphology. In this study, equilibrium was obtained about 3 h after the beginning of an experiment. Then, the flume was drained and the bed was fixed.

Three-dimensional flow velocities were measured using Acoustic Doppler Velocimetry (ADV) at a series of grid-defined points, which were taken in lines at four cross sections

(C1–C4), as shown in Fig. 2. In each line, the lowest measurement point is located at 5 cm above the bed due to the measuring requirements of the ADV, and other points are located in the line with a vertical interval of 1 cm. The ADV equipment, Nortek Vectrino + , is able to measure flow velocity up to 4 m/s with an accuracy of ± 1 mm/s. The sampling frequency is 100 Hz and data are collected over a duration of 120 s. In the processing of flow velocities, the backscattered signal strength or the signal-to-noise ratio for each ADV beam is used for quality control (see Yuan et al. for details [29]). Bed elevation is measured by a handheld laser rangefinder with an accuracy of ± 0.1 mm.

2.2 Numerical model description

The Reynolds Averaged Navier–Stokes Equations (RANS) and contaminant transport equations are used for the 3D numerical model (ANSYS FLUENT 14.0):

$$\rho \left[\frac{\partial \bar{u}_i}{\partial t} + \frac{\partial}{\partial x_j} (\bar{u}_i \bar{u}_j) \right] = - \frac{\partial \bar{p}}{\partial x_i} + \frac{\partial}{\partial x_i} \left[\mu \left(\frac{\partial \bar{u}_i}{\partial x_j} + \frac{\partial \bar{u}_j}{\partial x_i} \right) \right] + \frac{\partial}{\partial x_i} (-\rho \overline{u_i u_j}) + \rho g_i \tag{1}$$

$$\frac{\partial C}{\partial t} + \frac{\partial u_i C}{\partial x_i} = \frac{\partial}{\partial x_i} \left(\frac{\nu_t}{\sigma_c} \frac{\partial C}{\partial x_i} \right) \tag{2}$$

where $i, j = 1, 2,$ and 3 represents the $x, y,$ and z direction, respectively; ρ is the water density; \bar{u}_i is the mean velocity component in the i direction; x_i is the coordinate in the i direction; t is the time; \bar{p} is the time-averaged pressure; μ is the fluid dynamic viscosity; $-\rho \overline{u_i u_j}$ is the time-averaged Reynolds shear stress, g_i is the gravitational acceleration in the i direction; C is the contaminant concentration; u_i is the instantaneous velocity component in the i direction; ν_t is the coefficient of turbulent viscosity; and σ_c is a constant with a value of 0.9.

In order to close the RANS equations, the time-averaged Reynolds shear stresses need to be modeled. The Reynolds stress model (RSM) is used in this study. As this model accounts for the effects of streamline curvature, swirl, rotation, and rapid changes in strain rate in a more rigorous manner than other one- or two-equation models (i.e. $k-\epsilon,$ Re-Normalization Group $k-\omega,$ $k-\omega,$ and Shear Stress Transport $k-\omega$), it has a greater potential to give accurate predictions for complex flows like the secondary flow and separation zone at channel confluences [30], and has been successfully used to predict flow structures at channel confluences [31]. In this model, the equation for the transport of the Reynolds stresses ($\overline{\rho u_i u_j}$) is [30]:

$$\frac{DR_{ij}}{Dt} = D_{ij} + P_{ij} + \Pi_{ij} + \Omega_{ij} - \epsilon_{ij} \tag{3}$$

where $R_{ij} = \overline{u_i u_j},$ D_{ij} is the transport of R_{ij} by diffusion, P_{ij} is the production rate of $R_{ij},$ Π_{ij} is the transport of R_{ij} due to turbulent pressure-strain interactions, Ω_{ij} is the transport of R_{ij} due to rotation, and ϵ_{ij} is the dissipation rate of $R_{ij}.$

$$D_{ij} = \text{div} \left(\frac{\mu_t}{\sigma_k} \nabla R_{ij} \right) \tag{4}$$

$$P_{ij} = - \left(R_{im} \frac{\partial U_j}{\partial x_m} + R_{jk} \frac{\partial U_i}{\partial x_m} \right) \tag{5}$$

$$\Pi_{ij} = - C_1 \frac{\varepsilon}{k} \left(R_{ij} - \frac{2}{3} k \delta_{ij} \right) - C_2 \left(P_{ij} - \frac{2}{3} P \delta_{ij} \right) \tag{6}$$

$$\Omega_{ij} = - 2\omega_k (R_{jm} e_{ikm} + R_{im} e_{jkm}) \tag{7}$$

$$\varepsilon_{ij} = 2/3 \varepsilon \delta_{ij} \tag{8}$$

where $\mu_t = \rho C_\mu \frac{k^2}{\varepsilon}$; σ_k , C_μ , C_1 , and C_2 are empirical constants with the values of 0.82, 0.09, 1.8, and 0.6, respectively; $P = \frac{1}{2} P_{kk}$; k , $m = 1, 2$, and 3 represents the x , y , and z direction, respectively; $\delta_{ij} = 1$ when $i = j$ and 0 when $i \neq j$; ω_k is the rotation vector; $e_{ijk} = 1$ if i, j , and k are in cyclic order and different, $e_{ijk} = -1$ if i, j , and k are in anti-cyclic order and different, and $e_{ijk} = 0$ in case that any two indices are the same.

The turbulent kinetic energy, $k = \frac{1}{2} \overline{u'_i u'_i}$, and the dissipation rate of turbulence kinetic energy, ε , are calculated from the following transport equations:

$$\frac{\partial \rho k}{\partial t} + \frac{\partial \rho \bar{u}_i k}{\partial x_i} = \frac{\partial}{\partial x_i} \left[\rho \left(\nu + \frac{\nu_t}{\sigma_k} \right) \frac{\partial k}{\partial x_i} \right] + \rho G_k - \rho \varepsilon \tag{9}$$

$$\frac{\partial \rho \varepsilon}{\partial t} + \frac{\partial \rho \bar{u}_i \varepsilon}{\partial x_i} = \frac{\partial}{\partial x_i} \left[\rho \left(\nu + \frac{\nu_t}{\sigma_k} \right) \frac{\partial \varepsilon}{\partial x_i} \right] + C_{\varepsilon 1} \rho \frac{\varepsilon}{k} G_k - C_{\varepsilon 2} \rho \frac{\varepsilon^2}{k} \tag{10}$$

where ν is the kinetic viscosity; $\nu_t = \frac{\mu_t}{\rho}$; $G_k = \nu_t \frac{\partial u_i}{\partial x_j} \left(\frac{\partial u_i}{\partial x_j} + \frac{\partial u_j}{\partial x_i} \right)$ is the source item of the turbulent kinetic energy k due to the mean velocity gradients; $C_{\varepsilon 1}$ and $C_{\varepsilon 2}$ are empirical coefficients with values of 1.44 and 1.92, respectively.

The finite-volume method is used to discretize the equations. A multi-block approach is used to draw the meshes, and the model is divided into four parts: main channel, tributary channel, confluence and downstream channel. The free water surface is traced by the volume of fluid (VOF) method. In the VOF method, the tracking of the interface between the phases is accomplished by calculating a continuity equation for the volume fraction of the water phase. The equation can be described as:

$$\frac{\partial F}{\partial t} + u_i \frac{\partial F}{\partial x_i} = 0 \tag{11}$$

where F is the volume fraction of the water phase, which is equal to 1 when the cell is full of water, 0 when the cell is empty, and a value between 0 and 1 when the cell is partially filled, respectively [30].

The meshes and boundary conditions are shown in Fig. 3. The inlet boundaries of tributary and main channels are divided into two parts in the vertical direction: velocity inlet and pressure inlet. The velocity inlet boundary conditions are used to define the velocity and scalar properties of the flow at inlet boundaries; while the pressure inlet boundary conditions are used to define the total pressure and other scalar quantities at flow inlets [30]. The separation line between the velocity inlet and the pressure inlet is determined based on the water level of each scenario. The downstream outlet boundary is also bifurcated. The bottom part is defined as a wall boundary to represent the tail gate, and the top part is defined as the pressure outlet boundary. The wall boundary conditions are used

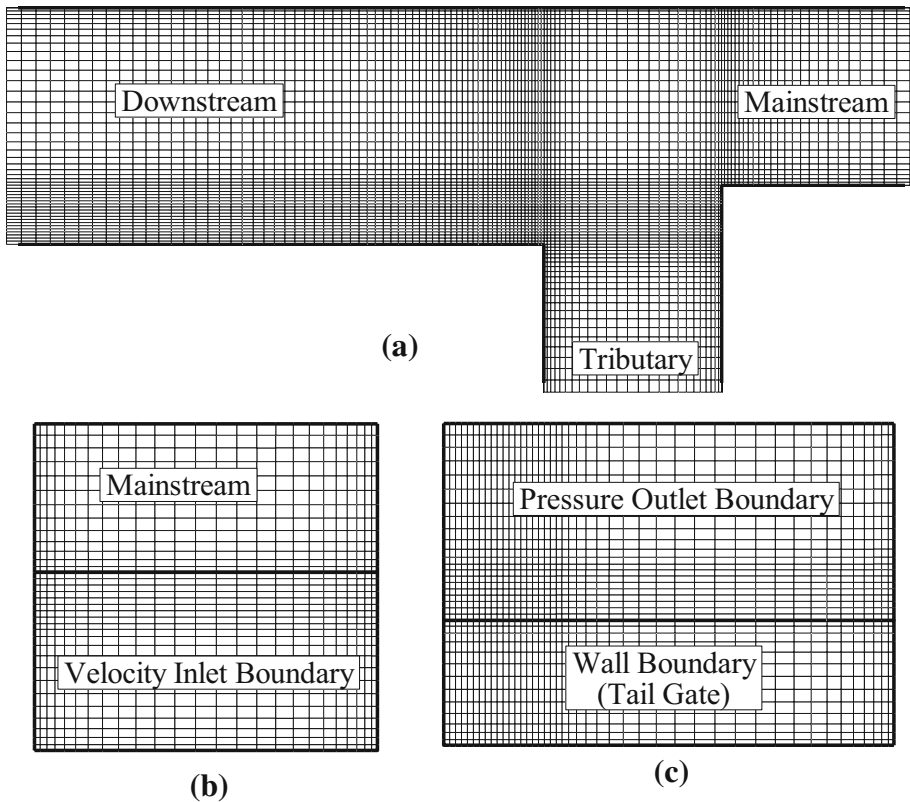


Fig. 3 Meshes and boundary conditions of the numerical model: **a** plan view of the channel confluence; **b** inlet cross section; **c** outlet cross section

to bound fluid and solid regions; while the pressure outlet boundary conditions are used to define the static pressure at flow outlets and also other scalar variables [30]. Contaminants are added in either mainstream or tributary channel by changing the species mass fractions of velocity inlet boundary to a proper number decided by different scenario settings. The meshes are mostly $1\text{ cm} \times 1\text{ cm} \times 1\text{ cm}$; those near the boundaries are finer with a size of $0.5\text{ cm} \times 0.5\text{ cm} \times 0.5\text{ cm}$; and those between the two parts are gradually changed. Fine meshes are also used in the regions where the separation zone and the shear layer are present due to complex flow patterns in these regions.

2.3 Simulation scenarios

Two distinct stabilized bed morphologies were obtained (Fig. 4). In Case 1, the bed morphology is characterized by the two deep scour holes caused by the spiral vortices at the downstream junction corner [10], and the shear flow [3] developed from the downstream junction corner oriented approximately 60 degrees to the inner bank of the downstream channel. Given the small discharge of the tributary flow, the shear flow is observed near the inner bank, and the two holes are not fully separated. The bed morphology is also characterized by the development of a depositional bar adjacent to the inner

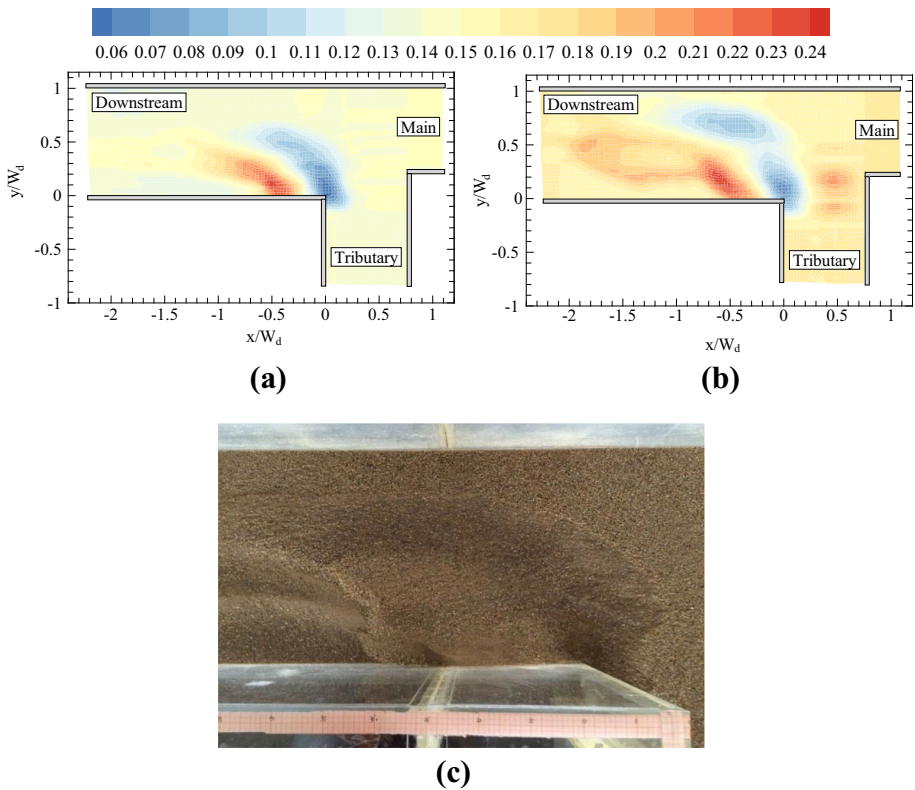


Fig. 4 Two degraded bed morphologies obtained in laboratory experiments: **a** contours of Case 1; **b** contours of Case 2; **c** photograph of fixed bed (The color band at the head represents relative bed elevation z/W_d)

bank. In Case 2, the same phenomena are also observed, except that the two deep scour holes are fully separated and the depositional bar is wider and longer than that in Case 1.

In order to analyze the effects of bed morphologies on the hydrodynamics and the transport of contaminants, eight scenarios are designed, as listed in Table 1.

2.4 Numerical model validation

To validate the numerical model, the velocities obtained at the same vertical lines of C1, C2, C3, and C4 from numerical and experimental results were compared. In Fig. 5, the horizontal axis represents the velocity magnitude, and the vertical axis represents the height of the channel. The velocity components in the streamwise, crosswise and vertical directions (U , V and W , respectively) were compared for two discharge ratios ($q = 2/3$ and $3/2$) and two locations ($y = 0.525 W_d$ and $y = 0.775 W_d$) in the mixing area. For the U component, the maximum error between numerical and experimental results is 16% at $y = 0.775 W_d$ of C2 and $q = 2/3$, and 24% at $y = 0.525 W_d$ of C2 and $q = 3/2$, respectively. It is also noted that the simulated errors of the rest points are less than 10% except for some points near the bed. For the V and W components, the simulated errors are relatively large, but the magnitudes of V and W components are very small, and thus they

Table 1 Scenarios for numerical simulation

Scenario	Discharge (L s^{-1})		Bed morphology	Contaminant concentration (mg L^{-1})	
	Tributary	Mainstream		Tributary	Mainstream
S1	6	9	Flat	100	0
S2	6	9	Degraded	100	0
S3	9	6	Flat	100	0
S4	9	6	Degraded	100	0
S5	6	9	Flat	0	100
S6	6	9	Degraded	0	100
S7	9	6	Flat	0	100
S8	9	6	Degraded	0	100

have a limited effect on the flow structure and mixing at channel confluences. In general, the numerical model is found to be suitable.

No physical modeling of contaminant transport was conducted due to the limitation of experimental facility. In a circulating flume, contaminants (e.g., phosphorus) can be easily dissolved in water soon after their addition into one of the upstream tanks, making it impossible to maintain a constant contaminant concentration in the tributary or main channel. Thus, no reliable concentration data of contaminants can be obtained from flume experiments to validate the distribution of contaminants. In this study, the distribution of contaminants at channel confluences was investigated using a 3D numerical model, ANSYS FLUENT 14.0, which was an efficient and reliable tool for simulating the transport and diffusion of contaminants in flows [32].

3 Results and discussion

3.1 Flow patterns at channel confluences with a flat or degraded bed

1. Streamwise velocity

Flow patterns at channel confluences are mainly characterized by six zones, including the zone of flow separation, shear layer, flow acceleration, flow recovery, flow deflection and flow stagnation [3, 4]. Leite Ribeiro et al. [10] further indicate that the tributary flow penetrates into the main channel mainly in the upper part of the water column due to bed discordance, whereas the lower part of the water column of the main channel flow is shielded by the bed discordance, giving rise to a two-layer flow structure in the confluence zone. In this study, these basic flow characteristics can also be found from the distribution of velocity components in the cross sections (Fig. 6). In S1 (Fig. 6a), the separation zone, whose border is defined as the zero velocity isoline of U [7], is located at the left side of the channel (view from upstream). The maximum width and length of the separation zone are about $0.15 W_d$ and $1.4 W_d$, respectively. Adjacent to the separation zone is the velocity acceleration zone resulting from the contraction of the two confluent flows by the separation zone. The maximum velocity can reach about 0.31 m/s, and the flow originating from the tributary and main channels occupies about 40 and 50% of the cross section, respectively. At the interface of the two incoming flows is the shear layer, which is characterized by a velocity gradient caused by the velocity difference between the two

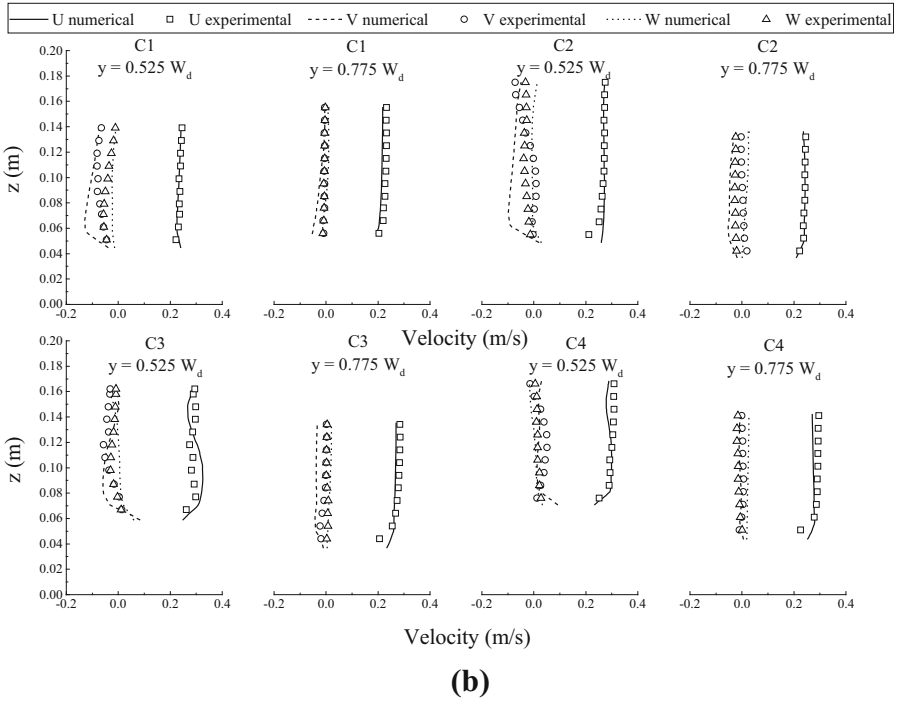
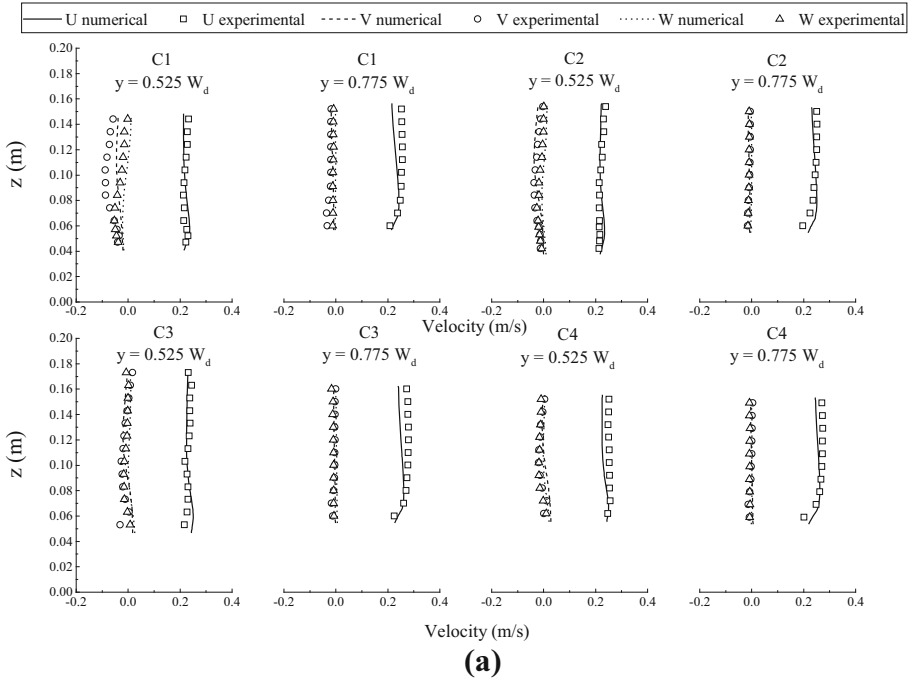


Fig. 5 Comparison of numerical (line) and experimental (marker) results of the velocity components in streamwise, crosswise and vertical directions in C1–C4: **a** scenario S2; **b** scenario S4

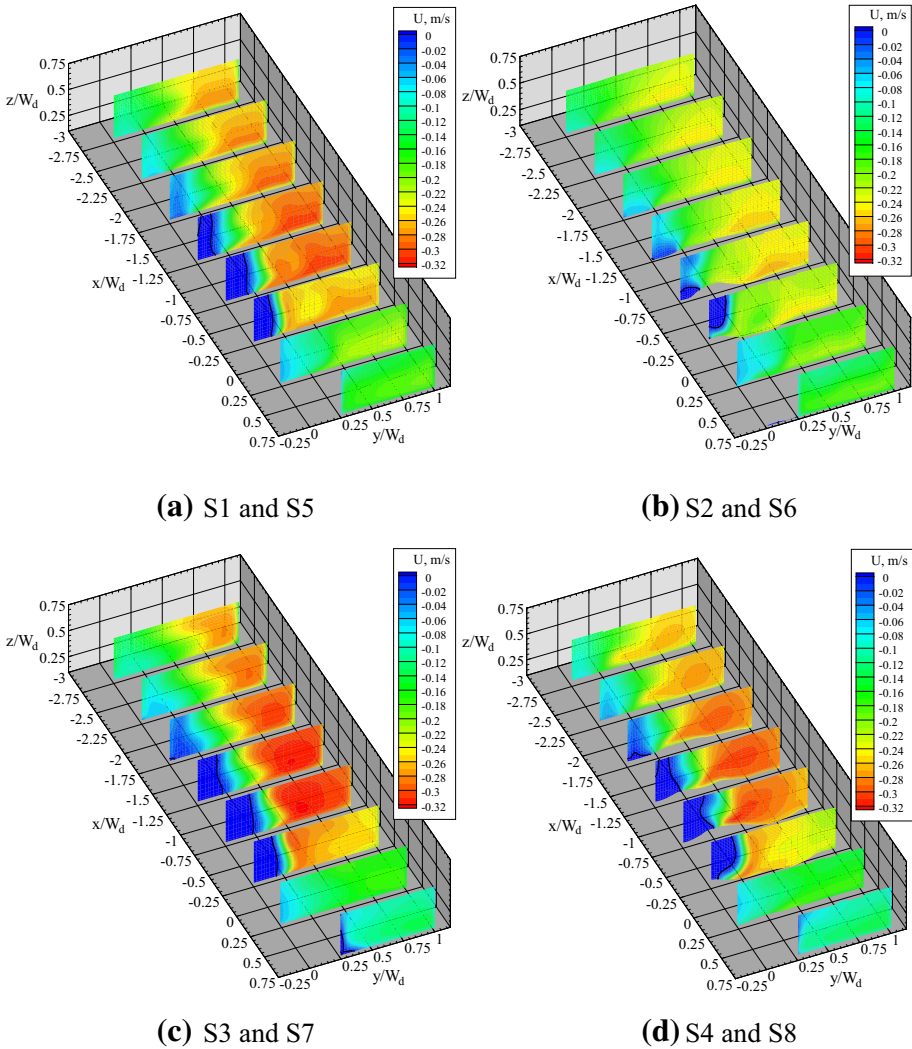


Fig. 6 Streamwise velocity distribution at channel sections downstream of the confluence (solid lines represent the border of the separation zone)

incoming flows [15, 33]. The shear layer is located at about $y/W_d = 0.5$, and its width increases as the shear layer disperses and dissipates in the downstream channel [22]. The flow patterns in other scenarios are generally the same as that in S1, except that the location and dimension of flow zones are different because of the differences in the discharge ratio and bed morphology.

The dimension of the separation zone increases as the discharge ratio increases, which is in agreement with the observations of Best and Reid [6]; and the shear layer moves towards the outer bank as its width increases. In scenario S3 with a large discharge ratio (Fig. 6c), the maximum width and length of the separation zone are increased to $0.2 W_d$ and $1.5 W_d$, respectively, and the maximum velocity is increased to 0.32 m/s because the velocity

acceleration zone contracts due to a larger separation zone. The shear layer moves from the middle of the channel to near the outer bank due to the increasing inflow momentum from the tributary.

Bed morphology affects not only the locations and dimensions of these zones, but also their deformation. For instance, the separation zone is present near the water surface and disappears near the bed; and the shear layer is distorted towards the tributary channel. The same phenomena are also observed in the studies of Biron et al. [5], Bradbrook et al. [16], and Wang and Yan [17]. The discharge ratio may also contribute to the effect of bed morphology on flow characteristics. In scenario S2 with a small discharge ratio (Fig. 6b), the degraded bed (Fig. 4a) leads to a decrease of the maximum width and length of the separation zone to $0.13 W_d$ and $0.55 W_d$, respectively. Moreover, the separation zone disappears below $z/W_d = 0.2$. As the size of the separation zone decreases, the maximum velocity decreases to 0.26 m/s. The shear layer is located above the deep scour hole and remains the same because the discharge ratios of S1 and S2 are the same. The distortion of the shear layer towards the deposition bar may be caused by the secondary circulation in the deep hole. An upwelling flow is observed at the inner side of the secondary circulation, which could prevent the penetration of tributary flow into the lower part of the water column of the main channel flow. This is like the effect of bed discordance on the shear layer [5]. In scenario S4 with a large discharge ratio (Fig. 6d), the size of the separation zone is almost the same as that in S3, while the border shape deforms according to the local bed morphology. The maximum velocity is similar to that in S3 as the sizes of the separation zones are almost the same. The deformation of the shear layer at a large discharge ratio is similar to that at a small discharge ratio, but its position is closer to the outer bank due to the larger contribution of the tributary discharge to the total discharge.

2. V – W vector field

Two counter-rotating helical cells can be found from the V – W vector plots for S1–S4 in Fig. 7, one of which is originated from the deflection of the tributary flow, and the other is initiated by the interaction between the tributary helical cell and the main channel flow [14]. In the extreme case of a symmetrical confluence, the flow originating from the main channel can also be deflected and two cells form. In other cases, one cell becomes stronger than the other cell [34]. Thus, the clockwise rotating helical cell is affected not only by the interaction between the tributary helical cell and the main channel flow, but also the deflection of the main channel flow. At $x/W_d = 0.25$ in S1 (Fig. 7a), the flow originating from the tributary channel penetrates into the confluence area from the left side with large relative positive V components. However, the magnitude of V components decreases as y/W_d increases. Due to the resistance of the main channel flow, the flow originating from the tributary channel is separated into an upwelling flow and a downwelling flow at about $z/W_d = 0.28$ and $y/W_d = 0.25$. At $x/W_d = -0.75$ (where ‘–’ indicates downstream of the confluence), the upwelling flow is extended to the tributary helical cell with counter-clockwise rotations, and occupies 2/3 of the upper water depth. The downwelling flow is extended to the main channel helical cell with clockwise rotations at the bottom. However, these two helical cells diminish at about $x/W_d = -0.75$. In some previous studies, helical cells were observed at both sides of the shear layer [35]; while in this study, helical cells are located at the upper and bottom portions of the water column. This may be because a small width to depth ratio and a large tributary discharge can induce distortion of the shear layer, and cause the special vertical distribution of helical cells found in this study [13].

An increase in the discharge ratio leads to the formation of stronger and more distinguishable helical cells [14]. In this study, the upper counter-clockwise tributary helical cell,

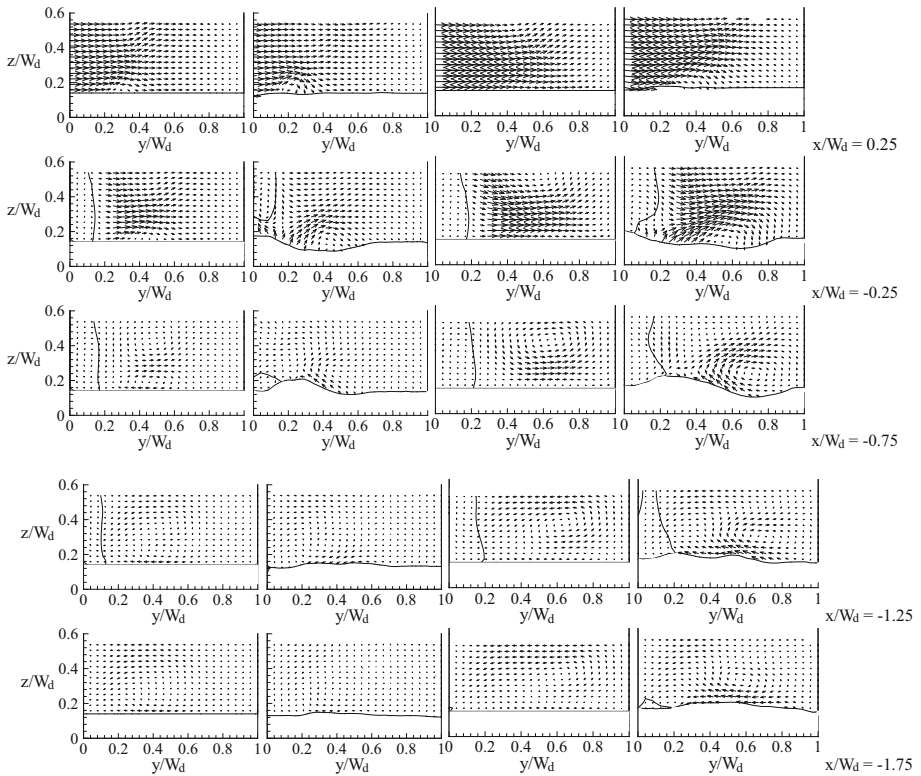


Fig. 7 *V*–*W* vector fields (view from upstream; row 1–4 represents S1–S4 or S5–S8 respectively; solid lines represent the border of the separation zone; Reference vector:0.2)

which owes its origin to the deflection of the tributary flow, tends to be stronger and moves to $y/W_d = 0.6$ with increasing discharge ratio, as the tributary flow penetrates deep into the main channel, and thus its deflection curvature increases. The starting position of the upwelling flow is extended to $y/W_d = 0.5$. The tributary helical cell develops and finally occupies the whole water depth, while the main channel helical cell shrinks dramatically but will not disappear due to the presence of negative *V* components near the bed.

Bradbrook et al. [16] showed that bed discordance could increase the intensity of secondary circulation and the mixing of flow. However, complex bed morphology (depositional bar and deep scour hole) at channel confluences may also induce flow redistribution and changes in the intensity of the two helical cells as shown in Figs. 7b, d. At $x/W_d = 0.25$, the local bed morphologies of S2 and S4 are similar, and the distribution of *V*–*W* vectors in S2 and S4 seems to be the same as that in S1 and S3, respectively. Downstream of $x/W_d = -0.25$, the discharge area increases because of the presence of a deep scour hole, and more water flows into the hole. The resistance caused by the flow originating from the main channel decreases, resulting in the disappearance of the upwelling flow and an increase in the intensity of the main channel helical cell. Obviously, for either flat or degraded bed, the strongest helical cell is formed in the shear layer where the deep scour hole is located. The main channel helical cell above the deep scour hole induces a downwelling flow directed towards the deepest point at the right side slope and an

upwelling flow directed towards the depositional bar near the inner bank at the left side slope. This may be one reason for the formation of the distinct bed morphology, deep scour hole and depositional bar at channel confluences [3, 10].

3.2 Transport of contaminants at channel confluences

The mixing of contaminants at channel confluences can be highly affected by the flow characteristics and bed morphology, which can be explained by three mechanisms, including (1) flow shear at the interface of confluent flows [36], (2) helical motions [4, 37], and (3) bed discordance [20, 21, 38].

1. Contaminants invade confluence from the tributary channel

Figure 8 depicts the distributions of contaminant concentrations at sections along the streamwise direction. Apparently, the distributions of contaminants are distinctive due to

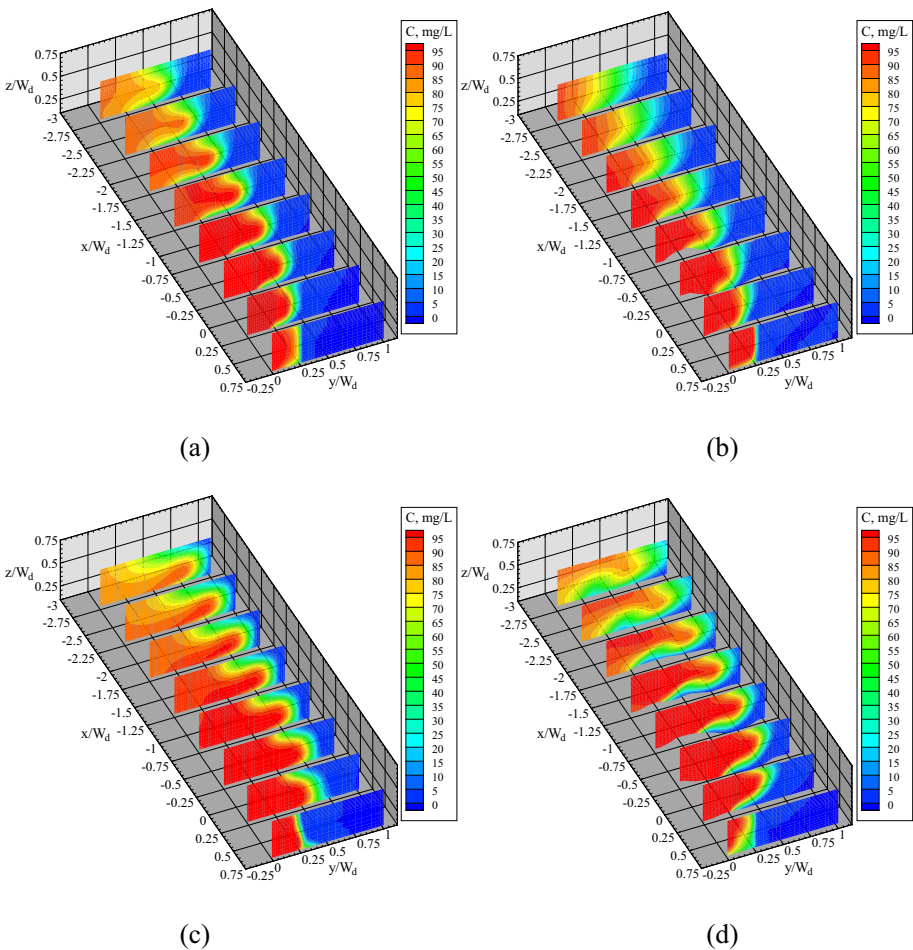


Fig. 8 The distribution of contaminant concentrations when water from the tributary channel is polluted (a–d represent S1–S4, respectively)

different flow characteristics for different scenarios. In all scenarios, there is a bending band with a large gradient of contaminant concentration at the interface between polluted and clean water, which is named the mixing layer [22]. In S1 (Fig. 8a), the mixing layer is located at $y/W_d = 0.4$, at which the shear layer is also located, and its width is about $0.2\text{--}0.3 W_d$ at $x/W_d = 0.25$. At the downstream sections, the mixing layer moves to the middle of the channel and its width increases. The shape of the mixing layer is convex, with the apex located approximately at the interface of the two helical cells. As the flow moves downstream, the convexity of the mixing layer increases for the relatively large positive V components at the interface of the two helical cells. As a consequence, contaminants move from the tributary channel into the clean water, and the flow with negative V components near the water surface and bottom pushes the clean water to dilute polluted water. The contaminated zone at the left side of the mixing layer is originated from the tributary channel with a high contaminant concentration, and it occupies about $1/3$ of the channel width in the upstream channel and half channel width in the downstream channel. The width of the right part, where there is clean flow originated from the main channel, shrinks from $1/2$ to $1/3$ of the channel width as the flow travels downstream.

The discharge ratio can affect the flow patterns and the mixing of contaminants at channel confluences. Biron et al. [38] showed that the mixing was slightly enhanced for a concordant bed as the discharge ratio increased. In the current study, the width of the mixing layer is increased to about $0.2\text{--}0.4 W_d$, indicating the stronger diffusion of contaminants at the mixing interface. Due to the increase of the discharge ratio, more polluted water penetrates into the main channel. The mixing layer nearly reaches the outer bank and deforms more dramatically, with the apex located near the bed, and it occupies nearly $3/4$ of the water depth. Meanwhile, the contaminated zone is enlarged, while the right part shrinks.

Bed discordance should be responsible for the rapid mixing at channel confluences [20, 38, 39]. In the current study, it is also found that bed morphology with a deep scour hole and separation bar can affect the mixing and distribution of contaminants at channel confluences. The comparison of contaminant distribution in S2 (Fig. 8b) and S1 (Fig. 8a) at a smaller discharge ratio shows that the location of the mixing layer remains largely unchanged, the width increases, and the convexity for S2 is not as high as that for S1. This is because the degraded bed can enhance the intensity of helical cells and the mixing in the mixing layer. The scope of the right part remains constant because the penetration distance of the tributary inflow into the mainstream is mainly controlled by the discharge ratio. Moreover, the contaminated zone (the left part) in S2 is smaller than that in S1 due to the increase of the width of the mixing layer. However, given a larger discharge ratio, the shape of the mixing layer in S4 (Fig. 8d) is notably different from that in S3 (Fig. 8c), and the apex of the mixing layer is upwelled to the water surface and occupies the upper $3/4$ of the water depth. Thereafter, the contaminated zone and the right part deform greatly due to the different shape of the mixing layer. Essentially, the helical cells with different locations and rotation directions contribute to different shapes of the mixing layer, and thus different distributions of contaminants at channel confluences.

2. Contaminants invade confluence from the main channel

The distributions of contaminant concentrations when the polluted water is discharged from the main channel are shown in Fig. 9. The water can also be separated into three parts, including the mixing layer at the interface between the clean and polluted water, the clean water (left part), and the polluted water (right part). The proportions of the three parts at each section are almost the same as that in Fig. 8. However, the clean water at the left

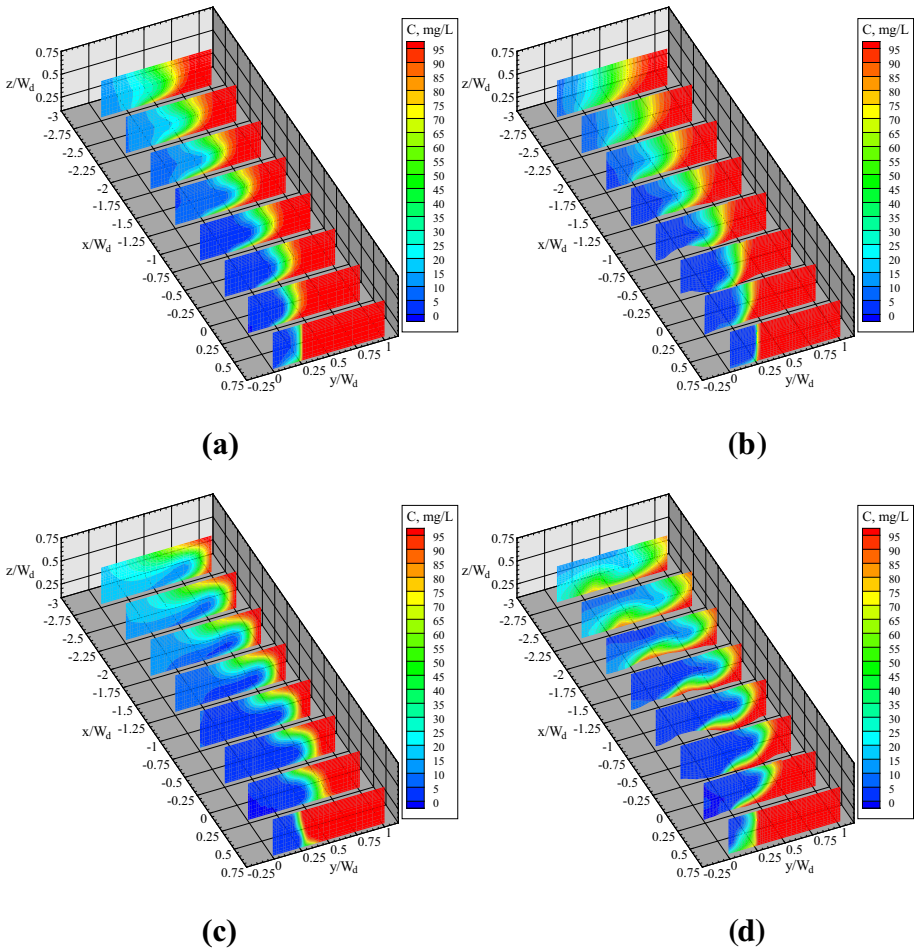


Fig. 9 The distribution of contaminant concentrations when polluted water is discharged only from the main channel (a–d represent S5–S8, respectively)

side is easier to pollute in the downstream channel, which can be attributed to the flow towards the inner bank driven by the relatively low pressure in the separation zone. Thus, the mixing area is extended to the left side of the channel. Biron et al. [38] also noted that the pressure gradient was a dominant control of the flow dynamics and mixing at confluences.

3. Deviation from complete mixing

The mixing rate is often used to characterize the mixing at channel confluences [20, 38, 39]. In this study, a non-uniformity index, the deviation from complete mixing [20], is used to assess the mixing rate and the redistribution of contaminants downstream of the confluence. This can be defined as:

$$Dev(x) = \sum_y \frac{|C_s(x, y) - C_p|}{C_p}$$

where $C_s(x, y)$ is the average simulated concentration of contaminants at the vertical line at (x, y) , and C_p is the flow weighted average predicted concentration [20], which is defined as:

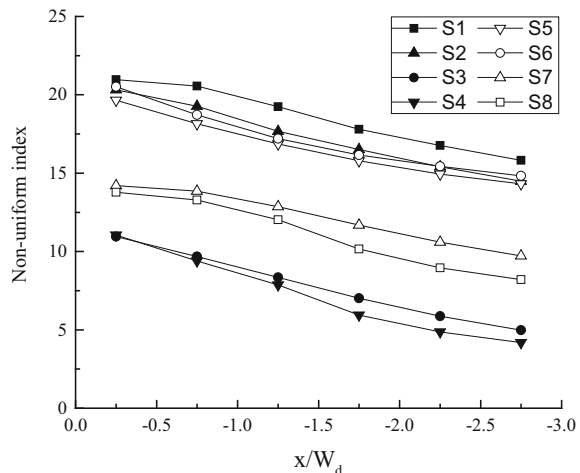
$$C_p = \frac{C_t Q_t + C_m Q_m}{Q_t + Q_m}$$

where C_t and C_m are the contaminant concentration in the tributary and main channel; Q_t and Q_m are the discharge in the tributary and main channel, respectively.

$Dev(x)$ for different scenarios is shown in Fig. 10. A lower $Dev(x)$ indicates a more uniform distribution of contaminants (more complete mixing). At a small discharge ratio, the line slopes of S1 and S2 are approximately the same, indicating that their mixing rates are almost the same. However, contaminants are more uniformly distributed in S2 than in S1, because the more complex bed morphology in S2 induces higher-intensity turbulence, which can enhance the mixing rate of contaminants at channel confluences. However, at a larger discharge ratio, the mixing is faster in S4 than that in S3. The difference of the non-uniformity index between the two discharge ratios indicates that a larger discharge ratio results in a quicker mixing process, so that the distribution of contaminants downstream could reach a uniform condition more quickly.

When contaminants invade the confluence from the main channel (S5–S8), the relation between S7 and S8 is the same as that between S3 and S4. The non-uniformity index of S5 is smaller than that of S6, indicating a faster mixing of contaminants for S5. This may be because of the larger velocities for S5 in the area where there is a transport path of pollutants and the relatively low pressure in the separation zone could entrain more polluted water to the left side of the channel, so that the contaminants can be transported to the downstream channel more easily and dispersed in the crosswise direction in S5.

Fig. 10 Non-uniformity index, i.e. the deviation from complete mixing, for the distribution of contaminants at downstream sections of each scenario



4 Conclusions

In this study, a 3D numerical model based on Reynolds Averaged Navier–Stokes equations and Reynolds Stress Turbulence model, is used to analyze the flow patterns and contaminant transport at confluences for different bed morphologies and discharge ratios. The results indicate that the mixing of contaminants can be strongly affected by flow patterns, which in turn can be affected by the discharge ratio and bed morphology at channel confluences. Several conclusions can be drawn from this study:

1. The mixing of contaminants occurs mainly at the interface of the two confluent flows in the mixing layer. The location of the mixing layer is related to the shear flow, and its formation is affected by the distribution and development of helical cells.
2. As the discharge ratio increases, the shear flow moves towards the outer bank, the counter-clockwise tributary helical cell caused by the deflection of the tributary flow occupies almost the whole cross section, and the mixing is enhanced in accompany the motion towards the outer bank and the distortion of the mixing layer.
3. Bed morphology has an effect on the mixing through the formation of the shear layer. With the presence of the deep scour hole and separation bar, the clockwise main channel helical cell develops to be dominant at each cross section and a more rapid mixing occurs.
4. Contaminants originating from the main and tributary channels have their own transport paths.

In addition, the confluence angle may also be an important factor affecting the flow patterns and contaminant transport at channel confluences, which will be the focus of our future study.

Acknowledgements This research was funded by National Science Foundation of China (Grand Nos. 51239003, 51509073 and 51779080), the Research Innovation Program for Graduate Students of Jiangsu Province (Grand No. B1504703), and the Program of Introducing Talents of Discipline to Universities (111 Project, Grand No. B17015). The opinions and conclusions described in this paper are solely those of the authors and do not necessarily reflect the opinions or policies of the sponsors. Thanks are also extended to Huaihe River Basin Water Resources Protection Bureau for their support during the experiments. The authors are grateful to the anonymous reviewers for comments that helped improve the paper.

References

1. Schindfessel L, Creëlle S, Mulder TD (2015) Flow patterns in an open channel confluence with increasingly dominant tributary inflow. *Water* 7(9):4724–4751
2. Best, JL (1985) Flow dynamics and sediment transport at river channel confluences. Ph.D. Thesis, University of London
3. Best JL (1987) Flow dynamics at river channel confluences: Implications for sediment transport and bed morphology. In: Ethridge FG, Flores RM, Harvey MD (eds) Recent developments in fluvial sedimentology, vol 39. SPEM Publication, Tulsa, pp 27–35
4. Best JL (1988) Sediment transport and bed morphology at river channel confluences. *Sedimentology* 35:481–498
5. Biron P, Best JL, Roy AG (1996) Effects of bed discordance on flow dynamics at open channel confluences. *J Hydraul Eng* 122(12):676–682
6. Best JL, Reid I (1984) Separation zone at open-channel junctions. *J Hydraul Eng* 110(11):1588–1594
7. Yang QY, Wang XY, Lu WZ, Wang XK (2009) Experimental study on characteristics of separation zone in confluence zones in rivers. *J Hydrol Eng* 14(2):166–171

8. Constantinescu G, Miyawaki S, Rhoads B, Sukhodolov A, Kirkil G (2011) Structure of turbulent flow at a river confluence with momentum and velocity ratios close to 1: insight provided by an eddy-resolving numerical simulation. *Water Resour Res* 47:W05507. <https://doi.org/10.1029/2010WR010018>
9. Constantinescu G, Miyawaki S, Rhoads B, Sukhodolov A (2012) Numerical analysis of the effect of momentum ratio on the dynamics and sediment-entrainment capacity of coherent flow structures at a stream confluence. *J Geophys Res* 117:F04028. <https://doi.org/10.1029/2012JF002452>
10. Leite Ribeiro M, Blanckaert K, Roy AG, Schleiss AJ (2012) Flow and sediment dynamics in channel confluences. *J Geophys Res* 117:F01035. <https://doi.org/10.1029/2011JF002171>
11. Biron P, De Serres B, Roy AG, Best JL (1993) Shear layer turbulence at an unequal depth channel confluence. In: Clifford NJ, French JR, Hardisty J (eds) *Turbulence: Perspectives on Flow and Sediment Transport*. Wiley, Chichester, pp 197–213
12. Rhoads BL, Sukhodolov AN (2004) Spatial and temporal structure of shear layer turbulence at a stream confluence. *Water Resour Res* 40:W06304. <https://doi.org/10.1029/2003WR002811>
13. Yuan SY, Tang HW, Xiao Y, Qiu XH, Zhang HM, Yu DD (2016) Turbulent flow structure at a 90-degree open channel confluence: accounting for the distortion of the shear layer. *J Hydro-Environ Res* 12:130–147
14. Shakibainia A, Tabatabai MRM, Zarrati AR (2010) Three-dimensional numerical study of flow structure in channel confluences. *Can J Civ Eng* 37:772–781
15. De Serres B, Roy AG, Biron PM, Best JL (1999) Three-dimensional structure of flow at a confluence of river channels with discordant beds. *Geomorphology* 26:313–335
16. Bradbrook KF, Lane SN, Richards KS, Biron PM, Roy AG (2001) Role of bed discordance at asymmetrical river confluences. *J Hydraul Eng* 127:351–368
17. Wang XG, Yan ZM (2007) Three-dimensional simulation for effects of bed discordance on flow dynamics at Y-shaped open channel confluences. *J Hydrodyn* 19(5):587–593
18. Boyer C, Roy AG, Best JL (2006) Dynamics of a river channel confluence with discordant beds: flow turbulence, bed load sediment transport, and bed morphology. *J Geophys Res* 111:F04007. <https://doi.org/10.1029/2005JF000458>
19. Jirka GH (2004) Mixing and dispersion in rivers. In: Greco M, Carravetta A, Della Morte R (eds) *River Flow*. Taylor & Francis Group, London, pp 13–27
20. Gaudet JM, Roy AG (1995) Effect of bed morphology on flow mixing length at river confluences. *Nature* 373:138–139
21. Best JL, Roy AG (1991) Mixing-layer distortion at the confluence of channels of different depth. *Nature* 350:411–413
22. Mignot E, Vinkovic I, Doppler D, Riviere N (2014) Mixing layer in open-channel junction flows. *Environ Fluid Mech* 14(5):1027–1041
23. Mcguirk JJ, Rodi W (1978) A depth-averaged mathematical model for the near field of side discharges into open-channel flow. *J Fluid Mech* 86(4):761–781
24. Weerakoon SB, Tamai N (1989) Three dimensional calculation of flow structure in channel confluences using boundary-fitted coordinates. *J Hydrosoci Hydraul Eng* 7:51–62
25. Weerakoon SB, Tamai N, Kawahara Y (2003) Depth-averaged flow computation at a river confluence. *J Water Marit Eng* 156(1):73–83
26. Bradbrook KF, Biron PM, Lane SN, Richards KS, Roy AG (1998) Investigation of controls on secondary circulation in a simple confluence geometry using a three-dimensional numerical model. *Hydrol Process* 12:1371–1396
27. Bradbrook KF, Lane SN, Richards KS, Biron PM, Roy AG (2000) Large eddy simulation of periodic flow characteristics at river channel confluences. *J Hydraul Res* 38(3):207–215
28. Ferguson R, Hoey T (2008) Effects of tributaries on main-channel geomorphology. In: Rice SP, Roy AG, Rhoads BL (eds) *River confluences, tributaries and the fluvial network*. Wiley, England, pp 183–208
29. Yuan SY, Li L, Amini F, Tang HW (2014) Turbulence measurement of combined wave and surge overtopping over a full scale HPTRM strengthened levee. *J Waterw Port C* 4:04014014
30. ANSYS-FLUENT® (2011) User's Guide Release 14.0 (online). FLUENT Documentation. ANSYS Inc. <http://www.ansys.com>
31. Mohammadi S, Neyshabouri SAAS, Naser G, Vahabi H (2016) Numerical investigation of submerged vane effects on flow pattern in a 90° junction of straight and bend open channels. *Iran J Sci Technol Trans Civ Eng* 40(4):349–365
32. Wei J, Li R, Kang P, Liu SY (2012) Study on transportation and diffusion characteristics of contaminants at flow confluence. *Adv Water Sci* 23(6):822–828 (**In Chinese**)
33. Rhoads BL, Sukhodolov AN (2008) Lateral momentum flux and the spatial evolution of flow within a confluence mixing interface. *Water Resour Res* 44:W08440. <https://doi.org/10.1029/2007WR006634>

34. Weerakoon SB, Kawahara Y, Tamai N (1991) Three dimensional flow structure in channel confluence of rectangular section. In: Proceeding X XIV congress, international association for hydraulic research, Part A, 373–380
35. Rhoads BL, Sukhodolov AN (2001) Field investigation of three-dimensional flow structure at stream confluences: 1. Thermal mixing and time-averaged velocities. *Water Resour Res* 37:2393–2410. <https://doi.org/10.1029/2001WR000316>
36. Sukhodolov AN, Rhoads BL (2001) Field investigation of three-dimensional flow structure at stream confluences: 2. Turbulence. *Water Resour Res* 37:2411–2424. <https://doi.org/10.1029/2001WR000317>
37. Bradbrook KF, Lane SN, Richards KS (2000) Numerical simulation of three-dimensional time-averaged flow structure at river channel confluences. *Water Resour Res* 36:2731–2746. <https://doi.org/10.1029/2000WR900011>
38. Biron PM, Ramamurthy AS, Han S (2004) Three-dimensional numerical modeling of mixing at river confluences. *J Hydraul Eng* 130(3):243–253
39. Lane SN, Parsons DR, Best JL, Orfeo O, Kostaschuk RA, Hardy RJ (2008) Causes of rapid mixing at a junction of two large rivers: Río Paraná and Río Paraguay, Argentina. *J Geophys Res* 113:F02019. <https://doi.org/10.1029/2006JF000745>